

Deafness mutation in the MYO3A motor domain impairs actin protrusion elongation mechanism

Laura K. Gunther, Joseph A. Cirilo Jr., Rohini Desetty, and Christopher M. Yengo*

Department of Cellular and Molecular Physiology, College of Medicine, Pennsylvania State University, Hershey, PA 17033

ABSTRACT Class III myosins are actin-based motors proposed to transport cargo to the distal tips of stereocilia in the inner ear hair cells and/or to participate in stereocilia length regulation, which is especially important during development. Mutations in the *MYO3A* gene are associated with delayed onset deafness. A previous study demonstrated that L697W, a dominant deafness mutation, disrupts *MYO3A* ATPase and motor properties but does not impair its ability to localize to the tips of actin protrusions. In the current study, we characterized the transient kinetic mechanism of the L697W motor ATPase cycle. Our kinetic analysis demonstrates that the mutation slows the ADP release and ATP hydrolysis steps, which results in a slight reduction in the duty ratio and slows detachment kinetics. Fluorescence recovery after photobleaching (FRAP) of filopodia tip localized L697W and WT *MYO3A* in COS-7 cells revealed that the mutant does not alter turnover or average intensity at the actin protrusion tips. We demonstrate that the mutation slows filopodia extension velocity in COS-7 cells which correlates with its twofold slower *in vitro* actin gliding velocity. Overall, this work allowed us to propose a model for how the motor properties of *MYO3A* are crucial for facilitating actin protrusion length regulation.

Monitoring Editor

Michael Murrell
Yale University

Received: May 7, 2021

Revised: Oct 7, 2021

Accepted: Nov 8, 2021

INTRODUCTION

The stereocilia of inner ear hair cells are composed of highly cross-linked actin filaments that share a similar parallel actin bundle core with other actin-based protrusions including microvilli and filopodia. Interestingly, stereocilia are unique in that their actin filaments are extremely stable and must be maintained at a precise length throughout a lifetime (Manor and Kachar, 2008). In the cochlea, each hair cell generates a bundle of stereocilia (hair bundle) which includes three rows of stereocilia that form a staircase pattern and are linked together by transmembrane cadherin molecules (tip links). The distal tips of the stereocilia also contain the mechano-electrical transduction channel that is responsible for the electrophysiological response of the hair bundles when they tilt in response to a stimulus (Holt *et al.*, 2014). Although many different players have been iden-

tified, the mechanism of stereocilia length regulation during development and in mature hair cells is still unclear.

Vertebrate class III myosins exist in two isoforms, myosin 3A and myosin 3B (*MYO3A* and *MYO3B*) (Dosé and Burnside, 2000). Expression of class III myosins has been noted in several sensory as well as nonsensory tissues; however, expression is highest in the retina and inner ear (Dosé and Burnside, 2002). It is proposed that *MYO3A/B* are important for regulating the stereocilia length during development and that disrupting their function can lead to stereocilia degeneration and deafness (Walsh *et al.*, 2002, 2011; Ebrahim *et al.*, 2016; Lelli *et al.*, 2016). Specifically, *MYO3A* has been found to harbor mutations that are associated with nonsyndromic deafness (DFNB30) (Walsh *et al.*, 2002) and *MYO3B* is thought to be able to partially compensate for the lack of *MYO3A* function (Manor *et al.*, 2012). Studies with inner ear hair cells have found that *MYO3A* is important for the regulation of stereocilia length, spacing, and thickness (Salles *et al.*, 2009; Ebrahim *et al.*, 2016; Lelli *et al.*, 2016).

The domain structure of vertebrate class III myosins consists of an N-terminal kinase domain, followed by a conserved motor domain, a neck domain containing two calmodulin-binding IQ motifs, and a class-specific C-terminal tail region (Dosé *et al.*, 2003). The class-specific tail region contains a conserved tail homology domain 1, known to bind espin (ESPN) isoforms, which are proposed to be transported to the tips of actin protrusions by class III myosins to

This article was published online ahead of print in MBoC in Press (<http://www.molbiolcell.org/cgi/doi/10.1091/mbc.E21-05-0232>) on November 17, 2021.

*Address correspondence to: Christopher M. Yengo (cmey11@psu.edu).

Abbreviations used: FRAP, fluorescence recovery after photobleaching; MORN4, membrane occupation nexus repeat 4; *MYO3A*, myosin 3A; *MYO3B*, myosin 3B; TIRF, total internal reflection fluorescence.

© 2022 Gunther *et al.* This article is distributed by The American Society for Cell Biology under license from the author(s). Two months after publication it is available to the public under an Attribution-NonCommercial-Share Alike 4.0 International Creative Commons License (<http://creativecommons.org/licenses/by-nc-sa/4.0>).

“ASCB,” “The American Society for Cell Biology®,” and “Molecular Biology of the Cell®” are registered trademarks of The American Society for Cell Biology.

induce elongation (Salles *et al.*, 2009; Merritt *et al.*, 2012). MYO3A contains a longer tail domain, which contains a binding site for the adapter protein called membrane occupation and recognition nexus repeat containing 4 (MORN4) and a binding site for actin referred to as tail homology domain 2. MORN4 is proposed to anchor MYO3A to the plasma membrane of protrusion tips and thus stabilize its localization (Mecklenburg *et al.*, 2015; Li *et al.*, 2019). However, cargo transport is a controversial topic with class III myosins since MYO3A/3B knockout mice still demonstrated tip localization of ESPN-1 and MORN4 (Lelli *et al.*, 2016). MYO3A/3B knockout mice also displayed stereocilia with irregular lengths (e.g., some even more elongated with disrupted staircase patterns) and widths, suggesting MYO3A/B may be able to serve as an important control of stereocilia elongation especially during development (Lelli *et al.*, 2016). Interestingly, we reported that class III myosins allow slow controlled elongation of actin protrusions in a cell culture model, further suggesting they can prevent rapid uncontrolled elongation which could be crucial during development and formation of the precise staircase pattern of stereocilia (Raval *et al.*, 2016). We have characterized deafness-associated mutations in the motor domain of MYO3A that impact its motor ATPase and force-generating properties (Grati *et al.*, 2016; Dantas *et al.*, 2018), while it is unclear how the impaired motor properties disrupt MYO3A function at the tips of actin protrusions.

The myosin ATPase mechanism has been characterized in detail and has been found to be fairly conserved across the myosin superfamily (De La Cruz and Ostap, 2004; Geeves, 2016) (Scheme 1). Briefly, myosin binding to ATP triggers a weak actin-binding conformation that dissociates it from actin, and ATP hydrolysis typically occurs while myosin is detached from actin. When myosin with the hydrolyzed products in the active site binds to actin, it triggers the power stroke that is associated with force generation and the release of phosphate. Myosin remains tightly bound to actin until the release ADP allows a new ATP molecule to bind and restart the cycle. Currently, it is thought that by varying the rate constants of key steps within the conserved ATPase cycle, each myosin can be finely tuned for their physiological function (Heissler and Sellers, 2016a). For example, the duty ratio, which is defined as the fraction of the ATPase cycle that myosin is strongly bound to actin, dictates whether a myosin can function as a single molecule transporter (high duty ratio) or work in teams to generate force through interacting with actin filaments (low duty ratio motor).

Class III myosins have several interesting features of their ATPase cycle that have been studied with and without the kinase domain. Kinetic studies of MYO3A containing the kinase domain demonstrated extremely slow ATP binding, while phosphate release is fast and ADP release is relatively slow (Dosé *et al.*, 2007). MYO3A lacking the kinase domain showed a twofold higher maximum ATPase rate when compared with the construct containing a kinase domain (Dosé *et al.*, 2008). The faster ATPase activity was promoted by a faster ADP release rate constant and a shift in the rate-limiting step to ATP hydrolysis. *In vitro* motility of MYO3A lacking the kinase domain and containing the full neck domain (2 IQ domains) revealed that actin-gliding is relatively slow but consistent with detachment limited models (Salles *et al.*, 2009; Raval *et al.*, 2016). Therefore, MYO3A displays properties of a high duty ratio motor, fast Pi-release, and slower ADP release, while the slow ATP binding and hydrolysis steps are very different from other high duty ratio myosins that function as transporters.

In a previous study, we examined a dominant mutation (L697W) in the MYO3A gene that causes a hearing loss phenotype (Grati *et al.*, 2016; Dantas *et al.*, 2018). We found that the L697W mutation causes

a decrease in actin protrusion length, but can outcompete the WT protein at the tips of actin protrusions in the presence of ESPN-1. *In vitro* motor function studies demonstrated that the L697W mutation decreases maximum actin-activated ATPase activity, enhances steady-state actin affinity, and decreases actin sliding velocity in the motility assay. Therefore, we concluded that the mutant can localize to the stereocilia tips but since it has an impaired motor it is unable to properly perform its length regulation function.

The goal of the current study was to examine the key steps in the MYO3A motor ATPase cycle that are impacted by the L697W mutation, providing crucial information about how the mutation impairs MYO3A force generation and/or cargo transport. Our biochemical characterization and a complementary cell biological analysis allowed us to examine how the impaired motor properties impact the ability of MYO3A to mediate actin protrusion length and dynamics. The results have allowed us to develop a working model of how MYO3A impacts actin-protrusion length regulation and further understand how deafness mutations alter this process. Overall, we propose that the MYO3A motor is tuned to generate force at protrusion tips, which allows it to play a crucial role in coordinating actin protrusion elongation and length.

RESULTS

Steady-state ATPase

In our previous study we examined the actin-activated ATPase of L697W and WT MYO3A containing the motor and calmodulin-binding IQ domains but lacking the kinase domain (MYO3A Δ K 2IQ) and reported the impact of the mutation on the maximum ATPase rate (V_{Max}) as well as the actin concentration at which ATPase is half maximal (K_{ATPase}). We noticed the K_{ATPase} was extremely low for the mutant and thus in the current study we performed ATPase experiments at even lower actin concentrations (0.1, 0.5, 1 μ M actin). Our results demonstrate the K_{ATPase} is reduced 10- to 20-fold in the mutant. The V_{Max} was reduced ~4-fold in the mutant similar to our previous work. We also measured the steady-state ATPase rate as a function of temperature (25, 30, and 35°C) at saturating actin (20 μ M) (Figure 1). Slopes of the temperature-dependent ATPase measurements were similar between WT (6.43 ± 0.04) and L697W (6.91 ± 0.34), suggesting a similar rate-limiting step in the mutant and WT constructs.

Basal ATPase activity

To further examine the ATPase rate in the absence of actin, we utilized the malachite green assay that measures the liberation of phosphate as a function of time. The ATPase activity (moles of inorganic phosphate per moles myosin) was plotted versus time and fitted with a linear regression (Figure 2). The basal ATPase activity of MYO3A Δ K 2IQ L697W (0.33 ± 0.03) was about threefold higher than WT MYO3A Δ K 2IQ (0.11 ± 0.01), which was similar to the results from the NADH assay. Since phosphate release is rate limiting in the absence of actin (Dosé *et al.*, 2007, 2008), this step may be accelerated by the mutation.

ATP-binding

We examined the rate of ATP binding to MYO3A Δ K 2IQ in the absence of actin using mant-labeled ATP and unlabeled ATP as previously described (Dosé *et al.*, 2007, 2008). We mixed MYO3A Δ K 2IQ (0.5 μ M) with 5 μ M mantATP and varying concentrations of unlabeled ATP in the stopped-flow. The increase in mantATP fluorescence as a function of time was monitored and fit to a two exponential function at all ATP concentrations. We observed a fast phase that was independent of ATP concentration and a slow

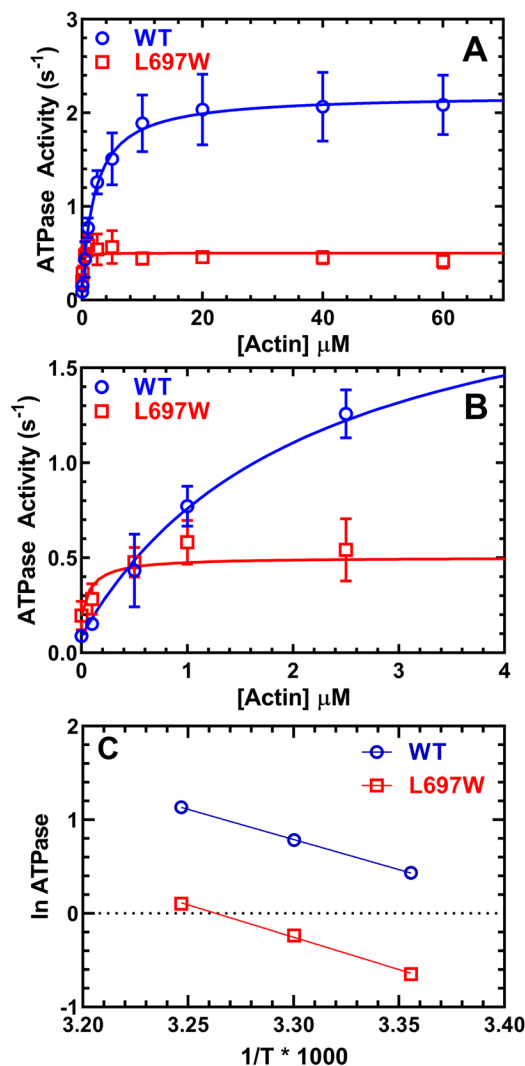


FIGURE 1: Steady-state ATPase properties. (A) The ATPase activity was monitored as a function of actin concentration in WT and L697W. The data were fit to the Michaelis–Menten relationship to determine the maximum ATPase activity (V_{Max}) and actin concentration at which ATPase activity is one-half maximal (K_{ATPase}). (B) The ATPase activity of L697W is shown at lower actin concentrations to highlight the extremely low K_{ATPase} value. (C) The ATPase activity was also measured as a function of temperature in the presence of 20 μM actin. The Eyring plot demonstrates a similar temperature dependence of ATPase for the mutant and WT. Data in A and B represent the average ($\pm\text{SD}$) from three separate protein preparations.

phase that was dependent on ATP concentration (Figure 3). The relative amplitude of the slow phase varied between 50 and 70% of the total fluorescence signal. On average the fast phase was five-fold faster in the mutant than the WT. The slow phase was linearly dependent on ATP concentration and used to determine the second-order binding constant for ATP binding (K_1k_2), which was quite similar in L697W and WT MYO3A $\Delta\text{K 2IQ}$ (Table 1). The results suggest that there are two conformations of MYO3A $\Delta\text{K 2IQ}$ in the absence of actin for both WT and L697W. The fast phase may represent a conformation that has a weaker affinity for mantATP and thus dissociates rapidly, while the slow phase represents a conformation that binds mantATP with higher affinity and thus dissociates more slowly.

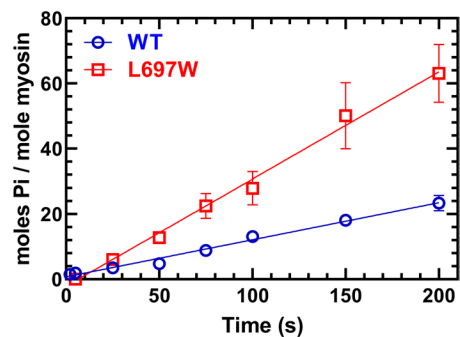


FIGURE 2: Basal ATPase activity. The ATPase activity in the absence of actin (v_0) was further examined using the malichite green assay to measure moles of phosphate produced per mole of myosin over a 200-s period. The ATPase activity in the absence of actin was threefold enhanced in the mutant compared with WT MYO3A $\Delta\text{K 2IQ}$. Data represent the average ($\pm\text{SD}$) from four separate protein preparations.

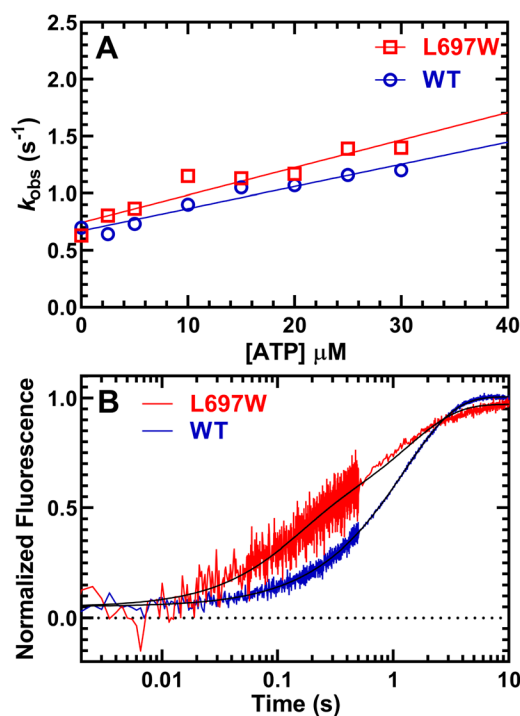


FIGURE 3: ATP binding to MYO3A $\Delta\text{K 2IQ}$. The rate of ATP binding was measured by kinetic competition with mantATP in the absence of actin. MYO3A $\Delta\text{K 2IQ}$ (0.5 μM) was rapidly mixed with mantATP (5 μM) and various concentrations of ATP. (A) Fluorescent transients at all ATP concentrations were fit to a double exponential. The fast phases were independent of ATP concentrations, while the slow phases were linearly dependent on ATP concentration. The average rate of the fast phase was enhanced fourfold in the mutant (2.6 ± 1.1 and 10.6 ± 1.7 , respectively). The second-order rate constant was determined from the slope of the linear dependence on the slow phase and was similar between WT and L697W (Table 1). (B) Representative fluorescence transients of 0.5 μM MYO3A $\Delta\text{K 2IQ}$ mixed with 5 μM ATP and mantATP and fit to a biexponential function.

ATP-induced dissociation from actin

The rate of ATP binding to acto-MYO3A $\Delta\text{K 2IQ}$ was examined by monitoring the change in light scatter upon ATP-induced dissociation of MYO3A $\Delta\text{K 2IQ}$ from actin (Figure 4). We mixed

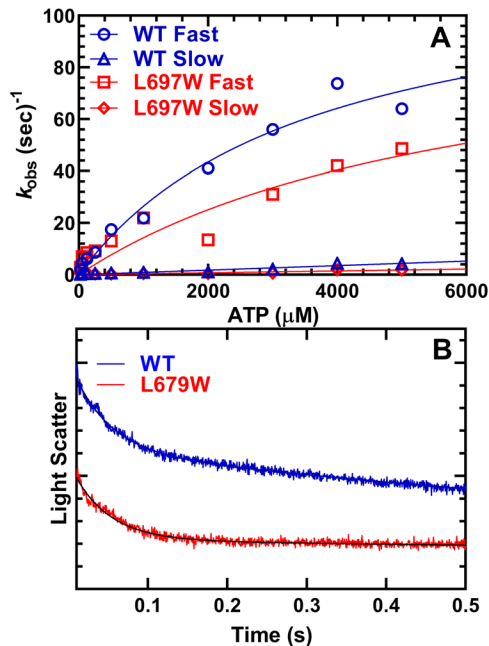


FIGURE 4: ATP-induced dissociation from actin. The rate of ATP binding to acto-MYO3A Δ K 2IQ was examined by monitoring the change in light scatter upon ATP-induced dissociation of acto-MYO3A. Transients were fit with two or three exponential function at all ATP concentrations. The fast phase represented ~40–50% of the total transient. (A) The fast phases were plotted vs. ATP concentration and fit to a hyperbolic relationship to determine the second-order rate constant for ATP binding ($K'_{1T}k'_{2T}$) and maximum rate of ATP-induced transition into the weak binding states (k'_{+2T}). The following equation was used to fit the hyperbolic dependence of k_{obs} on ATP concentration. $((K'_{1T}k'_{2T}[ATP])/(1+K'_{1T}[ATP]))$. (B) Representative fluorescence transients from mixing 0.5 μ M MYO3A Δ K 2IQ with 1 mM ATP and fit to a two exponential function.

acto-MYO3A Δ K 2IQ (0.5 μ M:0.25 μ M) with varying concentrations of ATP and observed two or three exponential light scatter transients at all ATP concentrations. The relative amplitude of the fast phase represented 40–50% of the total change in light scatter. The slower phases were not dependent on ATP concentration, which suggests that multiple conformations of the rigor conformation are possible as has been noted in other myosins (Geeves *et al.*, 2000; Greenberg *et al.*, 2015). The fast phase of the light scatter transient was hyperbolically dependent on ATP concentration and the maximum rate was used to determine the maximum rate of ATP-induced transition into the weak binding states (k_{+2}), while the ATP concentration dependence was used to evaluate the initial interaction between ATP and acto-MYO3A Δ K 2IQ (K_1). The second-order binding constant for ATP binding to acto-MYO3A Δ K 2IQ was determined from the linear dependence at low ATP concentrations. Overall, the rates of ATP binding to acto-MYO3A Δ K 2IQ were relatively unchanged by the mutation.

ADP dissociation in the presence of actin

The rate of ADP dissociation from acto-MYO3A Δ K 2IQ was measured by using mantADP. A complex of MYO3A Δ K 2IQ (0.5 or 0.375 μ M), 1 μ M actin, and 10 μ M mantADP was rapidly mixed with 1 mM ATP in the stopped-flow. The mantADP fluorescence transients were best fit with a two exponential function (Figure 5). The rate constant of the fast phase in the presence of actin was $10.3 \pm 0.1 \text{ s}^{-1}$ for WT and $4.2 \pm 0.1 \text{ s}^{-1}$ for L697W (relative

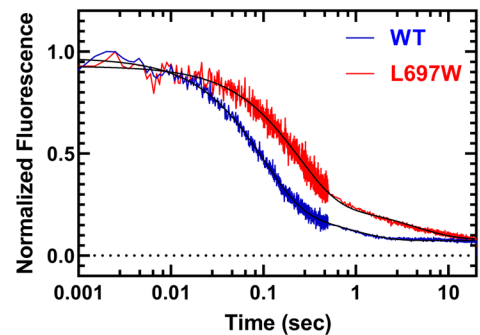


FIGURE 5: ADP dissociation from Acto-MYO3A Δ K 2IQ. The rate of ADP dissociation from MYO3A Δ K 2IQ was measured using mantADP in the presence of actin. A complex of MYO3A Δ K 2IQ (0.375–0.5 μ M), 1 μ M actin, and 10 μ M mantADP was rapidly mixed with 2 mM ATP in the stopped-flow. Fluorescence transients were best fit with a two exponential function. The rate constant of the fast phase in the presence of actin was $10.3 \pm 0.1 \text{ s}^{-1}$ for WT and $4.2 \pm 0.1 \text{ s}^{-1}$ for L697W (relative amplitudes 0.84 and 0.8, respectively). The slow phase was $1.1 \pm 0.1 \text{ s}^{-1}$ for WT and $0.2 \pm 0.1 \text{ s}^{-1}$ for L697W.

amplitudes 0.84 and 0.8, respectively). The slow phase was $1.1 \pm 0.1 \text{ s}^{-1}$ for WT and $0.2 \pm 0.1 \text{ s}^{-1}$ for L697W. The twofold decrease in the rate of mantADP release for L697W agrees well with the twofold decrease in vitro actin gliding velocity (54.8 ± 0.6 and $31.3 \pm 0.4 \text{ nm/s}$ for WT and L697W, respectively) (Dantas *et al.*, 2018).

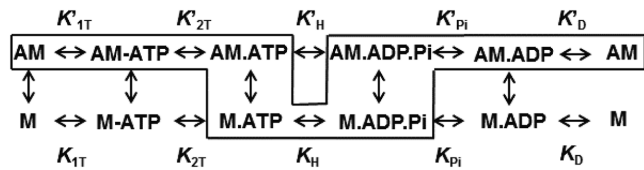
Single turnover measurements

A sequential mix experiment was performed by first mixing MYO3A Δ K 2IQ (0.8–1.0 μ M) with 10 μ M mantATP, allowing the reaction to age for 20 s, and then mixing with varying concentrations of actin (2.5–60 μ M) and 1 mM ADP (final conditions: 0.2–0.25 μ M MYO3A Δ K 2IQ, 2.5 μ M mantATP, 0.5 mM ADP, and 1.25–30 μ M actin). The fluorescence traces were fit to a single exponential function at all actin concentrations. The rate constants were plot as a function of actin concentration and fit to a hyperbolic function to determine the maximum rate (k_{MAX}) and actin concentration at which the rate was one-half maximal ($K_{0.5}$) (Figure 6). The k_{MAX} was similar to the ADP release rate constant (Table 1), suggesting phosphate release is fast and ADP release is slow for both WT and L697W.

Kinetic modeling and calculation of myosin duty ratio

We performed kinetic modeling of the WT and L697W ATPase cycles by developing a kinetic model of the entire ATPase cycle as represented in Scheme 1. Most of the rate constants included in the model were based on measured values (Table 1), while some were estimated based on how well the data fit to the steady-state ATPase results (e.g., ATP hydrolysis). The rate and equilibrium constants used in the model presented in Supplemental Table S1 and the simulated ATPase values, which were found to be quite similar to experimental values, are shown in Supplemental Figure S1. We estimated the duty ratio using an equation that takes into account the rate constants for ATP hydrolysis, phosphate release, and ADP release (Eq. 1) (Forgacs *et al.*, 2009). Previous estimates of duty ratio (~0.9) did not take into account the ATP hydrolysis step (Dosé *et al.*, 2007). We found that the estimated duty ratio was 30% reduced by the mutation (duty ratio ~0.2 and 0.3 for L697W and WT, respectively).

$$d_{ratio} = \left(\frac{k_{+H}k'_{Pi}}{k_{+H} + k'_{Pi}} \right) / \left(\left(\frac{k_{+H}k'_{Pi}}{k_{+H} + k'_{Pi}} \right) + k'_{D} \right) \quad (1)$$



SCHEME 1: Myosin ATPase cycle.

Filopodia extension and retraction dynamics

To examine the effect of the mutation on actin protrusion dynamics, we utilized COS-7 cells which do not endogenously express MYO3A or its binding partner Espin-1 (Schneider *et al.*, 2006). COS-7 cells were allowed to adhere to live-cell imaging petri dishes for 24 h before they were transfected with either full-length WT or L697W MYO3A Δ K containing an N-terminal GFP tag (Raval *et al.*, 2016; Dantas *et al.*, 2018). After 24 h of transfection, the cells were imaged using a Leica DMi8 total internal reflection fluorescence (TIRF) microscope containing a live-cell imaging chamber. The extension velocity of MYO3A-associated filopodia was examined in WT ($n = 100$ filopodia from 14 cells) and L697W

($n = 47$ filopodia from 12 cells) transfected cells by performing time-lapsed imaging (10-s frame rate). We also examined retraction velocities when they were observed while they were extremely rare for WT and not observed for L697W for the time periods recorded. We did not observe filopodia collapse or filopodia being overrun by the rest of the cell. The average extension velocity was 10.72 ± 4.58 nm/s for WT and 7.38 ± 3.76 nm/s for L697W (Figure 7). The decreased extension velocity for L697W correlates with the decreased in vitro motility velocity. The average filopodia length was significantly reduced in L697W compared with WT (Figure 7), as was also observed in our previous work (Dantas *et al.*, 2018).

Tip localization

We also examined the impact of the mutation on MYO3A tip localization efficiency by examining the same set of images collected above (Figure 8). Filopodia were randomly selected and line scans were generated by drawing a line that extended from just outside the filopodia tip to just within the cell body (see Supplemental Figure S2). We compared a similar number of filopodia containing WT (69 filopodia from 10 cells) and L697W (72 filopodia from

Steady-state ATPase values (\pm SE)	WT	L697W
v_0 (s^{-1}), $n = 4^a$	0.11 ± 0.01	$0.33 \pm 0.02^{**}$
v_0 (s^{-1}), $n = 3^b$	0.09 ± 0.01	$0.20 \pm 0.03^*$
V_{Max} (s^{-1}), $n = 3^b$	2.20 ± 0.08	$0.51 \pm 0.03^{**}$
K_{ATPase} (μM), $n = 3^b$	2.14 ± 0.35	$0.10 \pm 0.08^*$
Rate/equilibrium constants (\pm SE)	WT	L697W
ATP binding/hydrolysis (myosin), $n = 1^c$		
$K_{1T}k_{+2T}$ ($\mu M^{-1} \cdot s^{-1}$)	0.024 ± 0.003	0.019 ± 0.002
$k_{+H} + -H$ (s^{-1})	$\sim 3^\dagger$	N.D.
ATP binding (actomyosin), $n = 1^d$		
$K'_{1T}k'_{+2T}$ ($\mu M^{-1} \cdot s^{-1}$)	0.04 ± 0.01	0.03 ± 0.01
$K_{0.5}$ (μM)	3627 ± 1302	6258 ± 6311
k'_{+2T} (s^{-1})	122 ± 23	104 ± 67
Actin-activated phosphate release ^e		
$K_{0.5}$ (μM)	$29 \pm 4.0^\dagger$	N.D.
k_{+Pi} (maximum rate, s^{-1})	$74 \pm 5^\dagger$	N.D.
Actomyosin ADP release, $n = 3^f$		
k'_{+D} (s^{-1}) (fast phase)	10.3 ± 0.1	$4.2 \pm 0.1^{**}$
k'_{+D} (s^{-1}) (slow phase)	1.1 ± 0.1	$0.2 \pm 0.1^*$
Single turnover, $n = 3^f$		
$K_{0.5}$ (μM)	1.2 ± 0.5	0.5 ± 1.0
k_{MAX} (s^{-1})	11.1 ± 0.6	$3.3 \pm 0.7^{*,**}$

^aMalichite green assay.

^bNADH coupled assay.

^cCompetition with mantATP.

^dLight scatter.

^ePhosphate-binding protein.

^fmant-ADP.

** $p \leq 0.001$.

* $p \leq 0.05$.

[†]From Dosé *et al.* (2008).

[‡]Estimated from k_{obs} at 30 μM actin.

TABLE 1: Kinetic parameters of WT and L697W MYO3A Δ K 2IQ.

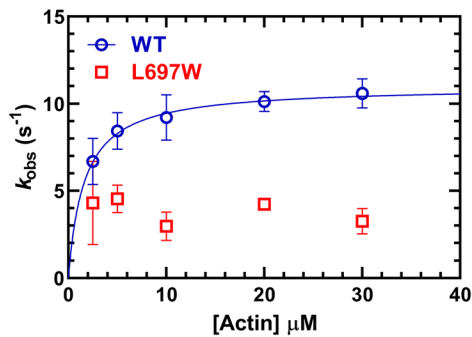


FIGURE 6: Single turnover measurements. Sequential mix experiments were carried out to monitor the single turnover rate of MYO3A Δ K 2IQ in the presence of actin. Fluorescence transients were fit to a single exponential function for both WT and L697W at all actin concentrations. The rate constants were plotted as a function of actin concentration and fit to a hyperbolic function for WT MYO3A Δ K 2IQ. The data for L697W did not fit well to a hyperbolic function but the rate constants were similar at each actin concentration. Each data point is the average (\pm SD) from three separate protein preparations.

15 cells) MYO3A. The tip-to-base ratio was found to be similar for WT and L697W-associated filopodia (Figure 8A). The peak fluorescence intensity had a very similar profile in WT and L697W-associated filopodia (Figure 8B). However, the frequency of filopodia that had a profile identical to the average fluorescence profile was slightly higher for L697W than WT, suggesting less variability between localization patterns for L697W MYO3A.

FRAP measurements of MYO3A Δ K tip dynamics

We examined the turnover of MYO3A at tips of stable filopodia by performing FRAP measurements. COS-7 cells that were transfected for 24 h with either WT or L697W full-length MYO3A Δ K were examined using a Leica SP8 confocal microscope. The tips of filopodia were bleached using a 488-nm laser for 25 s and the fluorescence was allowed to recover for 2000 s. The percentage of recovery was plotted versus time and fitted with a single exponential function. WT recovered with a half time of 1080 ± 90 s ($n = 57$ filopodia, $N = 18$ cells) and L697W recovered with a similar half time of 1065 ± 119 s ($n = 30$ filopodia, $N = 14$ cells). On average the

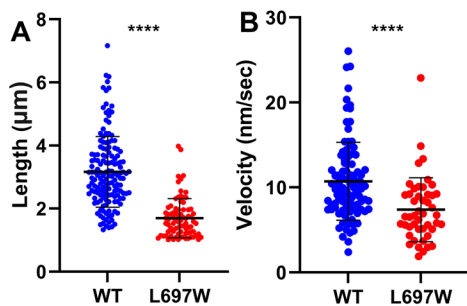


FIGURE 7: Filopodia length and dynamics. COS-7 cells were transfected with either WT or L697W GFP-MYO3A Δ K and the filopodia dynamics were examined by live-cell TIRF microscopy. (A) Scattered dot plot showing filopodia length for both WT and L697W. WT filopodia were significantly longer than L697W filopodia ($p < 0.0001$, mean values: WT = 3.16 ± 1.12 , L697W = 1.70 ± 0.62). (B) Scattered dot plot showing filopodia extension velocities for both WT and L697W. WT filopodia extended at a significantly faster velocity than L697W ($p < 0.0001$, mean values: WT = 10.72 ± 4.58 , L697W = 7.38 ± 3.76). Error bars are \pm SD.

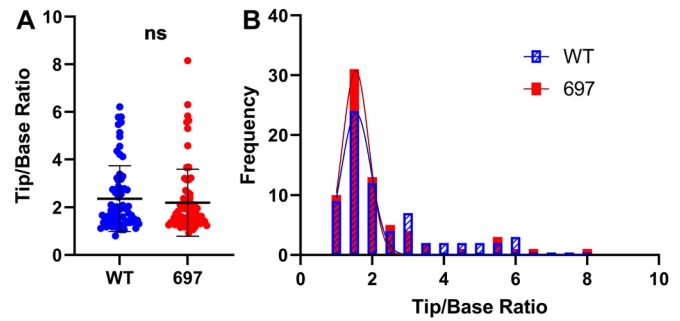


FIGURE 8: MYO3A filopodia tip localization. COS-7 cells were transfected with either WT or L697W GFP-MYO3A Δ K and the filopodia tip localization efficiency was analyzed. (A) Scattered dot plot showing tip/base ratios for both WT and L697W. There is no statistical difference between mean values ($p = 0.48$, mean values: WT = 2.36 ± 1.37 , L697W = 2.20 ± 1.41). Error bars are \pm SD. (B) Distribution of tip/base ratio fit to a Gaussian function. The mean value, representing the highest frequency tip/base ratio, was the same for both WT and L697W ($Z = 3.55$, mean values: WT = 1.55 ± 0.41 , L697W = 1.54 ± 0.37).

traces recovered close to 100% for both WT and L697W (1.13 ± 0.05 and 0.95 ± 0.06 s, respectively), and no immobile fraction was detected (Figure 9).

Full-length MYO3A tip localization and dynamics in the presence of MORN4

To further examine the impact of L697W in a more physiological context, COS-7 cells were transfected with a kinase-dead version of MYO3A (GFP MYO3A K50R) (Quintero *et al.*, 2010) with or without the L697W mutation in the motor domain. We also cotransfected with mCherry MORN4 since it enhances tip localization of full-length MYO3A (Mecklenburg *et al.*, 2015). Similar to our results with MYO3A Δ K, COS-7 cells transfected with either GFP MYO3A K50R (WT or L697W) and mCherry MORN4 displayed no significant difference in MYO3A tip localization efficiency. However, the average length of L697W MYO3A was significantly shorter than WT (WT, 10 cells and 144 filopodia; L697W, 10 cells and 136 filopodia) (Figure 10), consistent with the trend observed with the MYO3A Δ K constructs (Figure 7).

DISCUSSION

We performed a detailed characterization of the motor properties of MYO3A with a deafness mutation (L697W) in the motor domain and investigated the impact of the mutation on actin protrusion length/dynamics. It is well established that MYO3A is able to localize to the tips of actin protrusions, including stereocilia, microvilli, and filopodia, as well as promote the formation and elongation of these protrusions (Les Erickson *et al.*, 2003; Schneider *et al.*, 2006; Salles *et al.*, 2009; Quintero *et al.*, 2010; Ebrahim *et al.*, 2016; Raval *et al.*, 2016; Cirilo *et al.*, 2021). Our previous results demonstrated that the L697W mutant was still able to tip localize; however, it had a significantly decreased ability to induce and maintain the lengths of actin protrusions (Dantas *et al.*, 2018). Our current results demonstrate that the mutation not only impacts steady-state MYO3A ATPase activity but also specifically impacts detachment kinetics, which correlates well with the depressed *in vitro* actin gliding velocity we reported previously (Dantas *et al.*, 2018). Live-cell filopodia tracking showed that COS-7 cells transfected with the mutant MYO3A had decreased filopodia lengths and elongation rates when compared with WT counterparts. In addition, our FRAP results demonstrated

the mutation does not impact MYO3A turnover at the protrusion tips. Together, our results indicate that the L697W deafness mutation in MYO3A can properly localize to actin protrusion tips, but its impaired motor activity specifically causes a slowing of the actin protrusion elongation rate. Our results support a model in which MYO3A-associated force generation at the protrusion tips plays a role in coordinating actin protrusion elongation.

Impact of L697W on motor ATPase kinetics

In the current study we characterized the impact of the L697W deafness mutation on key steps in the MYO3A ATPase pathway. We found that while ATP binding is unchanged, the ADP release rate constant is decreased approximately twofold in the mutant. In the detachment-limited model of myosin motility, the ADP release rate constant limits the detachment rate of myosin from actin in the presence of saturating ATP (Siemankowski *et al.*, 1985). Thus, our ADP release results are in agreement with the *in vitro* motility and suggest both WT and L697W MYO3A follow a detachment limited model of motility. Interestingly, we propose that ADP release is not rate limiting in the WT and L697W ATPase pathways in solution and hypothesize that the ATP hydrolysis step is rate limiting. The hypothesis is supported by the single turnover data which demonstrate that MYO3A posthydrolysis has a turnover rate that is similar to the ADP release rate constant in both WT and L697W (Figure 6). Therefore, since the maximum ATPase rate is nearly 10-fold slower than the posthydrolysis single turnover rate, we propose ATP hydrolysis is at least partially rate limiting. Our kinetic modeling fits well with the measured and proposed rate and equilibrium constants presented in Table 1 and Supplemental Figure S1. We calculated the duty ratio based on the equation that takes into account the ATP hydrolysis and product release steps and found that L697W has a 30% lower duty ratio compared with WT. This is contrary to our results that found L697W has a twofold higher steady-state actin affinity than WT (Dantas *et al.*, 2018). Thus, we suggest that the mutant's decrease in ATP hydrolysis, which stabilizes the weak actin-binding states, and the reduced ADP release rate constant, which stabilizes the strong binding states, partially offset each other in terms of duty ratio. In addition, other factors such as the affinity for actin in the M.ATP state may account for the apparent discrepancies between the measured steady-state actin affinity and the calculated duty ratio.

A duty ratio of 0.3 for the WT MYO3A motor is not as high as the processive dimeric myosin motors such as MYO5A and MYO6 (De La Cruz and Ostap 2004), suggesting MYO3A may not function as a processive motor. However, MYO3A dimerization has not been investigated and there is no predicted coiled-coil in the tail domain. In addition, other factors may play a significant role in MYO3A translocation to the tips of protrusions, such as interactions of the tail domain with actin and/or the plasma membrane (see Merritt *et al.*, 2012; Cirilo *et al.*, 2021).

Impact of L697W on tip localization and turnover

We utilized FRAP to investigate the impact of the L697W deafness mutation on MYO3A turnover at the protrusion tips. We found no difference in the half time between WT and L697W MYO3A (Figure 9). These findings seem to contradict previous results that demonstrate MYO3A L697W can outcompete MYO3A WT at the tips of actin protrusions when both are present in COS-7 cells (Dantas *et al.*, 2018). However, the out-competition primarily was found in actin protrusions where ESPN-1 is present, a known binding partner of MYO3A. In our previous work we hypothesized that L697W MYO3A may be able to outcompete WT because of a higher duty

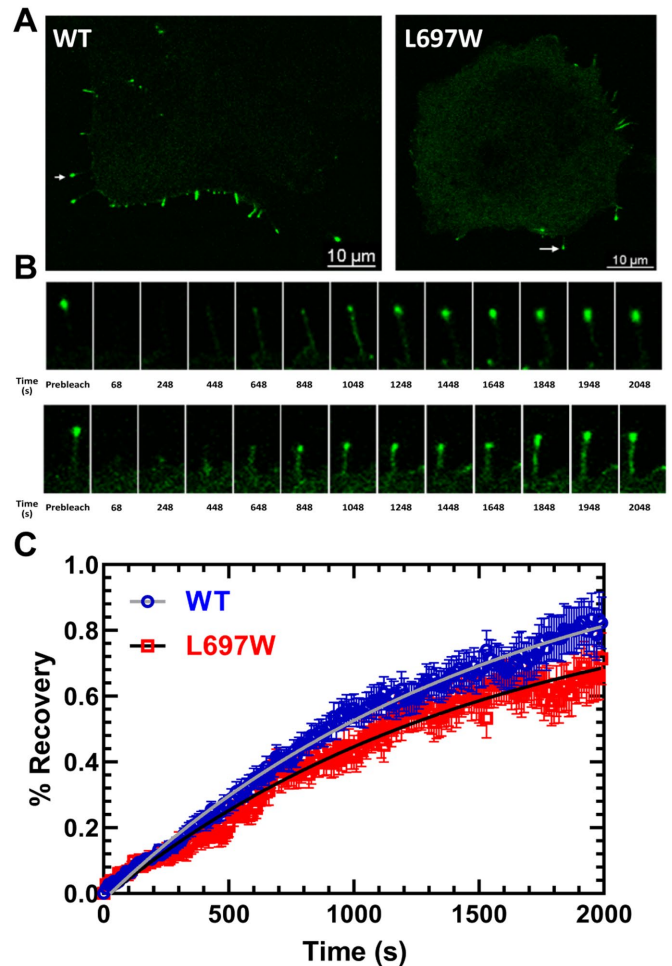


FIGURE 9: FRAP measurements of MYO3A Δ K turnover at filopodia tips. (A) Representative images of COS-7 cells transfected with GFP-tagged WT or L697W MYO3A Δ K. (B) FRAP was performed on COS-7 cell filopodia tips by bleaching for 25 s and monitoring the time course of fluorescence recovery for 2000 s (10-s frame rate) (WT, top panel, and L697W, bottom panel). (C) The fluorescence was normalized and the percentage of recovery was plotted vs. time and fitted with a single exponential function. WT recovered with a half time of 1080 ± 90 s ($n = 57$ filopodia, $N = 18$ cells) while L697W recovered with a similar half time of 1065 ± 119 s ($n = 30$ filopodia, $N = 14$ cells). The fraction of recovery was near 1 for both WT and L697W (1.13 ± 0.05 s and 0.95 ± 0.06 s, respectively), demonstrating that nearly 100% recovery was achieved in 2000 s and no immobile fraction detected. Error bars are \pm SEM.

ratio, while our current biochemical analysis demonstrates this is not likely the case. Therefore, we now propose that the competitive inhibition of WT MYO3A is dependent on the presence of ESPN-1 and the slower detachment kinetics of L697W. It is possible that L697W binds more tightly to ESPN-1 because it populates a specific biochemical state for a longer period of time (e.g., the actomyosin. ADP state), which stabilizes the complex at the tips. In addition, there may be other nonmotor factors that contribute to the tip localization of MYO3A, for example, formation of an autoinhibited state involving head-tail interactions, membrane-tail interactions, and other binding partners at the tip. Raval *et al.* (2016) demonstrated that COS-7 cells transfected with MYO3A constructs containing different regions of the tail deleted had depressed tip localization. Thus, the tail domain is an important aspect of tip localization, and

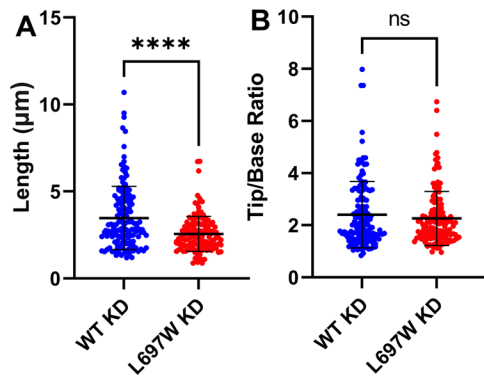


FIGURE 10: Filopodia length and tip localization in MYO3A full-length kinase-dead (KD) constructs. COS-7 cells were transfected with kinase-dead GFP-MYO3A WT or L697W and mCherry-MORN4. The filopodia length and tip localization were examined by live-cell TIRF microscopy. (A) Scattered dot plot showing filopodia length for both WT KD and L697W KD. WT KD filopodia were significantly longer than L697W KD filopodia ($p < 0.0001$, mean values: WT KD = 3.47 ± 1.81 , L697W KD = 2.56 ± 1.00). (B) Scattered dot plot showing tip/base ratios for both kinase-dead WT and L697W. There is no statistical difference between mean values ($p = 0.72$, mean values: WT KD = 2.40 ± 1.27 , L697W KD = 2.26 ± 1.04). Error bars are \pm SD.

its interactions with the membrane and other binding partners likely contribute to the turnover of MYO3A at the tips.

Measurements of actin protrusion elongation and length regulation

Length regulation in actin protrusions such as filopodia and stereocilia is dependent on numerous factors. Some important factors include actin polymerization/retrograde flow, membrane tension, as well as the presence of unconventional myosins along with their binding partners (Belyantseva *et al.*, 2003; Belyantseva *et al.*, 2005; Lin *et al.*, 2005; Rzadzinska *et al.*, 2005; Naoz *et al.*, 2008; Rzadzinska *et al.*, 2009; Salles *et al.*, 2009; Manor *et al.*, 2011; Merritt *et al.*, 2012; Drummond *et al.*, 2015; Narayanan *et al.*, 2015; Raval *et al.*, 2016; Avenarius *et al.*, 2017). Our current results highlight the importance of motor-based actin sliding in contributing to the elongation rate of actin protrusions. We emphasize that this is not due to the amount of MYO3A at the tips since the tip localization efficiency was similar in L697W and WT. The reduced average length of L697W-associated filopodia may be a result of the mutant having reduced force-generating capacity. Previous studies demonstrated that the presence of MYO3A at the tips of actin protrusions alters the protrusion dynamics compared with nontransfected or MYO10-transfected conditions (Raval *et al.*, 2016). These results support the hypothesis that motor activity directly correlates to protrusion elongation and length regulation (Raval *et al.*, 2016). However, the different tail domains in MYO3A and MYO10 could play a role in altering protrusion dynamics. Thus, the current study adds to our previous work by clearly demonstrating that disrupting the MYO3A motor properties, without altering the tail domain, can alter actin protrusion elongation and length regulation.

To further examine MYO3A-associated length regulation in a more physiological context, we examined the impact of the L697W mutation in a kinase-dead full-length construct in the presence of its binding partner MORN4. Our results demonstrate that the presence of the L697W mutant in full-length MYO3A causes a reduction in actin protrusion lengths without changing the tip localization efficiency (Figure 10), which mirrors our results in the

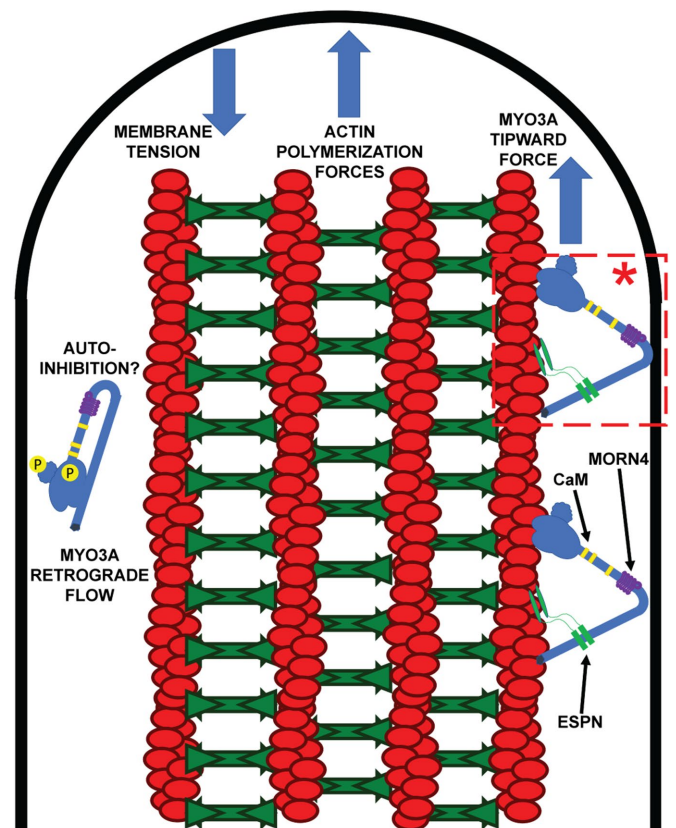


FIGURE 11: Model of MYO3A function in actin protrusions. MYO3A is able to walk to the tips of actin protrusions utilizing its motor domain and tail (THDII). MYO3A docks at the protrusion tips through an unknown mechanism (e.g., membrane-binding or protein-protein interactions) whereby both MYO3A and actin polymerization produce a tipward force that combats membrane tension allowing protrusion elongation. On accumulation at the tip, MYO3A undergoes autophosphorylation, which down-regulates motor activity* and results in MYO3A returning to the protrusion base via an unknown mechanism (e.g., autoinhibition and/or retrograde flow). Deafness-associated mutations in MYO3A may alter the number of MYO3A motors capable of tip localizing or the intrinsic force-generating capacity of MYO3A motors, which can alter the balance of forces at the tips of actin protrusions and disrupt length regulation.

kinase-deleted construct. Future studies will examine filopodia extension velocity of full-length MYO3A in the presence and absence of MORN as well as investigate the impact of MORN4 on in vitro motility.

Model of MYO3A-induced actin protrusion elongation

The results of our current study allow us to propose a model for how class III myosin motors participate in actin protrusion elongation and length regulation (Figure 11). In the case of MYO3A, we propose it localizes at the tips of actin protrusions and forms a link between the membrane and the actin bundle, analogous to what has been proposed in class I myosins in microvilli (Mooseker and Cheney, 1995; Tyska and Mooseker, 2002; Nambiar *et al.*, 2009). MYO3A can produce a tip-directed force by generating a power stroke that pushes the membrane toward the tip and resists the membrane tension inherent at the tips. The reduction in tip membrane tension allows the actin polymerization machinery to elongate the actin bundle and thus the protrusion. Therefore, the group of MYO3A motors at the tips functions as an ensemble of motors generating force to

Parameter	WT	L697W
Filopodia extension velocity (nm/s)	10.72 ± 4.58	7.38 ± 3.76**
Filopodia retraction velocity (nm/s)	10.45 ± 5.86	N/A
Filopodia length (µm)	3.16 ± 1.12	1.70 ± 0.62**
Filopodia tip/base ratio	2.36 ± 1.37	2.20 ± 1.41
FRAP recovery half time (s)	1080 ± 90	1065 ± 119
Fraction recovery	1.13 ± 0.05	0.95 ± 0.06

All values are mean (±SD), ** $p \leq 0.001$.

TABLE 2: Impact of WT and L697W MYO3A Δ K on actin protrusions in COS-7 cells.

resist the membrane tension, which is an important factor that mediates actin protrusion elongation and length. Upon accumulation at the tip, MYO3A undergoes autophosphorylation, which reduces its ATPase activity and affinity for actin (Quintero *et al.*, 2010, 2013). Therefore, it will be important to study how kinase-dependent MYO3A regulation impacts its ability to mediate actin protrusion elongation and length. Furthermore, since groups of MYO3A are seen moving toward the base (Quintero *et al.*, 2010), we speculate that MYO3A may adopt an autoinhibited conformation similar to what has been described for other members of the myosin superfamily (Heissler and Sellers, 2016b). We proposed that L697W has a slower elongation rate because of its reduced actin filament gliding velocity. In addition, L697W has a reduced average actin protrusion length because of a reduced ensemble force-generating capacity, which may be because of the reduced duty ratio or other factors that we did not measure such as intrinsic force and/or ability to adapt to external loads. Thus, future studies that can examine the intrinsic force generation and load sensitivity of single molecules of MYO3A will shed light on how force-generating capacity impacts actin protrusion length. In addition, most myosins that localize to actin protrusions (e.g., MYO1A, MYO7, MYO10, and MYO15) are proposed to associate with the membrane (Belyantseva *et al.*, 2003; Galdeen *et al.*, 2007; Yang *et al.*, 2009; Nambiar *et al.*, 2010; Moen *et al.*, 2011; Kerber and Cheney, 2011; Mazerik and Tyska, 2012; Mazerik *et al.*, 2014; Li *et al.*, 2017; Weck *et al.*, 2017) while no consensus membrane-binding motif has been identified in MYO3A/B. Therefore, another future direction will be to demonstrate that the MYO3A tail directly or indirectly interacts with the membrane.

There are several unconventional myosins found in stereocilia, while MYO3A/B and MYO15A are both known to regulate stereocilia length (Belyantseva, *et al.*, 2005; Schneider *et al.*, 2006; Salles *et al.*, 2009; Quintero *et al.*, 2010; Manor *et al.*, 2011; Ebrahim *et al.*, 2016; Lelli *et al.*, 2016; Rehman *et al.*, 2016; Krey *et al.*, 2020). Therefore, a key question is how do these two myosin motors work together to coordinate length regulation? The loss of MYO3A/B causes over elongation as was seen in the knockout mouse studies (Lelli *et al.*, 2016). In contrast, shaker 2 mice (MYO15sh2/sh2), which contain a mutation in a conserved cysteine residue, lack MYO15A tip localization and are associated with stereocilia that are of significantly shorter lengths (Rehman *et al.*, 2016; Krey *et al.*, 2020), further suggesting that MYO15A is crucial for stereocilia elongation. We suggest MYO3A and MYO15A may work together to produce and maintain stereocilia of a finite length. In the stereocilia, we propose that MYO15A and MYO3A are both able to produce a protruding force on the membrane at stereocilia tips. In addition, MYO15A has recently been shown to nucleate actin filaments (Moreland *et al.*, 2021). However, since MYO3A is the slower motor, it may function as a “brake” to

control the protrusion elongation rate, which in turn may prevent aberrant elongation and allow proper assembly of the components of the tip complex. The L697W MYO3A mutation leads to delayed onset deafness similar to what is observed in DFNB30. The slowed elongation with L697W MYO3A could impair stereocilia formation during development and/or maintenance and repair of mature stereocilia. Mouse model studies suggest that MYO3A is crucial during development (Lelli *et al.*, 2016), but no role for maintenance/repair has been established. The late onset phenotype suggests that there are compensatory mechanisms to make up for the loss of functional MYO3A that allow stereocilia to initially form and function normally. However, stereocilia must be maintained throughout a lifetime that likely requires proper turnover of crucial components of the actin bundle and tip complex (McGrath *et al.*, 2017). We propose that when MYO3A function is disrupted the compensatory mechanisms that allow the stereocilia to initially form during development may impair normal maintenance and repair of these unique and complex actin-based structures.

CONCLUSION

The current study characterized the impact of the deafness-associated L697W mutation in MYO3A using biochemical and cell biological studies. In the absence of its binding partner ESPN-1, the mutant does not alter actin protrusion tip localization efficiency and turnover at the tips, while the impaired motor activity causes slower elongation rates. Thus, our results allow us to propose a model that MYO3A generates protrusive forces to combat the membrane tension and works together with the actin polymerization-based forces to elongate the protrusions. Future studies will investigate how class III myosins coordinate with binding partners and MYO15A to regulate stereocilia lengths.

MATERIALS AND METHODS

[Request a protocol](#) through *Bio-protocol*.

Reagents

ATP and ADP were prepared fresh from powder and were purchased from Sigma. ATP and ADP concentrations were determined by absorbance at 259 nm using ϵ_{259} of 15,400 $M^{-1}\cdot cm^{-1}$. N-Methylanthraniloyl (mant)-labeled 2'-deoxy-ADP and 2'-deoxy-ATP were purchased from Jena Biosciences. The mantATP and mantADP concentrations were determined from absorbance measurements at 255 nm using ϵ_{255} of 23,300 $M^{-1}\cdot cm^{-1}$. Nucleotides were prepared prior to use in the presence of equimolar $MgCl_2$.

Construction of expression plasmids, protein expression, and purification

A construct of human MYO3A, containing 2IQ domains but lacking the kinase domain (MYO3A Δ K 2IQ; amino acids 340–1143 of NM_017433), a C-terminal GFP tag, and an N-terminal FLAG tag was engineered into pFastBac (Raval *et al.*, 2016). Another construct of human MYO3A containing the entire tail domain but lacking the kinase domain (MYO3A Δ K; amino acids 340–1616 of NM_017433) was introduced into the pEGFP plasmid, such that it contained an N-terminal GFP tag (Raval *et al.*, 2016). A MYO3A full-length construct containing the kinase-dead mutation (K50R) in pEGFP was also generated (Raval *et al.*, 2016). An mCherry MORN4 construct was previously described (Mecklenburg *et al.*, 2015). We used site-directed mutagenesis to introduce the L697W mutation into both the pFastBac and the pEGFP constructs (Dantas *et al.*, 2018). The mutant and WT MYO3A Δ K 2IQ

constructs were coexpressed with calmodulin using the insect SF9 cell baculovirus system and purified using anti-FLAG affinity chromatography (Quintero *et al.*, 2010; Quintero *et al.*, 2013). Actin was purified from acetone powder derived from rabbit skeletal muscle (Pell-Freeze) using the method of Pardee and Spudich (Pardee and Spudich, 1982).

Steady-state ATPase assay

The actin-activated ATPase activity of MYO3A Δ K 2IQ was examined using the NADH-coupled enzyme assay in KMg50 buffer (50 mM KCl, 1 mM EGTA, 1 mM MgCl₂, 1 mM ATP, 10 mM imidazole, pH 7.0, 1 mM dithiothreitol) at 25°C (De La Cruz, Sweeney, and Ostap 2000; Dosé *et al.*, 2007; Dosé *et al.*, 2008). The rate of ATPase activity was measured using an Applied Photophysics stopped-flow over a 200-s period and at varying actin concentrations. The ATPase rates were plotted as a function of actin concentration (0.1, 0.5, 1, 2.5, 5, 10, 20, 40, 60 μ M) and data were fit to a Michaelis–Menten equation ($V = v_0 + (k_{cat} \cdot [\text{actin}]) / (K_{ATPase} + [\text{actin}])$), which allowed determination of the maximum rate of ATPase activity (k_{cat}) and the actin concentration at which half maximal ATPase activity occurs (K_{ATPase}). Since the basal ATPase activity (v_0) was relatively high in the mutant, we reported the maximum ATPase activity (V_{Max}) as ($k_{cat} + v_0$) for comparing L697W and WT. The ATPase was also measured in the presence of 20 μ M actin at 20, 25, and 30°C to examine the temperature dependence of the steady-state ATPase.

Malachite green ATPase assay

Steady-state ATPase activity was measured using the malachite green assay (Lanzetta *et al.*, 1979). Briefly, WT or L697W MYO3A Δ K 2IQ was mixed with 1 mM ATP, allowed to hydrolyze for various time intervals, and quenched with 2N hydrochloric acid, and the inorganic phosphate levels were detected with malachite green. The malachite green absorbance was detected at 620 nm using an absorbance microplate reader (Thermo Multiskan Ascent). The concentration of inorganic phosphate was determined by a phosphate standard curve. All experiments were performed at 25°C. Data were plot as moles of phosphate per moles myosin as a function of time and fitted with a linear regression to determine the ATPase rate.

Transient kinetic experiments

All transient kinetic experiments were performed in an Applied Photophysics stopped-flow, with a dead time of 1.2 ms. Light scatter experiments were measured at 420 nm using a 395-nm long pass filter. Both mantATP and mantADP were excited via energy transfer from intrinsic tryptophans by exciting at 290 nm and measuring the emission through a 395-nm long pass filter. Fluorescence or light scatter transients were fit with software provided with the stopped-flow or Graphpad Prism software. All rate constants are reported with standard error of the fits unless indicated. All concentrations are given as the final concentration unless indicated. Kinetic modeling was performed using the ATPase pathway used in previous studies (Dosé *et al.*, 2007; Dosé *et al.*, 2008) and Kintek Explorer software.

COS-7 cell filopodia dynamics

COS-7 cells were trypsonized and plated (~40,000 cells) on imaging dishes (35 mm Azer Scientific) for 24 h in DMEM supplemented with 10% fetal bovine serum at 37°C and 5% CO₂ in a cell culture incubator. After 24 h, COS-7 cells were transfected with 2 μ g of pEGFP-MYO3A constructs (WT or L697W) using Lipofectamine transfection reagent (Invitrogen) and incubated for 24 h to allow overexpression. Cells were imaged in Opti-MEM media with no phenol red with ei-

ther a Leica DMi8 TIRF microscope or Leica SP8 confocal microscope equipped with a 37°C stage and objective warmer and 5% CO₂ chamber. Filopodia lengths were measured using the length tool in ImageJ. Filopodia that had clear extensions from the periphery of a cell were tracked using the Mtrack plugin.

Tip localization

Leica LASX software was used to generate line scans for each filopodia. In short, a line was drawn that extended from just outside the filopodia tip to just within the cell body. The fluorescence intensity of each line scan was normalized to the point with the highest intensity point for that filopodia, and the baseline was set by the linear fit to the fluorescence at the base. Line scans were then aligned by their highest point and averaged to develop a representative filopodia profile. Tip-to-base ratio for each filopodia was determined via dividing the highest intensity point for a filopodia by the fluorescence at the base of the filopodia.

FRAP

FRAP was performed by drawing a circular region of interest around the tip of a filopodia (average length of filopodia tip that was bleached was 2.43 ± 0.88 and 2.14 ± 0.71 μ m for WT and L697W, respectively). A 20-mW 488-nm laser line at 1% power was used to prebleach the region of interest every second for 20 s total to establish a steady-state intensity. We avoided using filopodia that exhibited a decrease in intensity during the prebleach. This was followed by 25 s of bleaching at 100% laser power and was then allowed to recover for 2000 s, while an image of the recovery was taken every 10 s. Filopodia were, on average, very stable during the 25 s of bleaching. The filopodia that reacted to the bleach were not used in the analysis. FRAP recovery traces for WT ($n = 57$ filopodia) and L697W ($n = 30$ filopodia) were averaged and fit to an exponential fit in Graph Pad Prism software.

Statistical analysis

The kinetic experiments were examined with an unpaired Student's *t* test (Table 1). The cell biological parameters were examined with a Mann–Whitney U test (Table 2 and Figure 10).

ACKNOWLEDGMENTS

This work was supported by a grant from PA Lions Hearing Research Foundation to C.M.Y. and National Institutes of Health Grant F32DC016788 to L.G.

REFERENCES

- Avenarius MR, Krey JF, Dumont RA, Morgan CP, Benson CB, Vijayakumar S, Cunningham CL, Scheffer DI, Corey DP, Müller U, *et al.* (2017). Heterodimeric capping protein is required for stereocilia length and width regulation. *J Cell Biol* 216, 3861–3881.
- Belyantseva IA, Boger ET, Friedman TB (2003). Myosin XVa localizes to the tips of inner ear sensory cell stereocilia and is essential for staircase formation of the hair bundle. *Proc Natl Acad Sci USA* 100, 13958–13963.
- Belyantseva IA, Boger ET, Naz S, Frolenkov GI, Sellers JR, Ahmed ZM, Griffith AJ, Friedman TB (2005). Myosin-XVa is required for tip localization of whirlin and differential elongation of hair-cell stereocilia. *Nat Cell Biol* 7, 148–156.
- Cirilo JA Jr, Gunther LK, Yengo CM (2021). Functional role of class III myosins in hair cells. *Front Cell Dev Biol* 9, e643856.
- Dantas VGL, Raval MH, Ballesteros A, Cui R, Gunther LK, Yamamoto GL, Alves LU, Bueno AS, Lezirovitz K, Pirana S, *et al.* (2018). Characterization of a novel MYO3A missense mutation associated with a dominant form of late onset hearing loss. *Sci Rep* 8, 8706.
- De La Cruz EM, Ostap EM (2004). Relating biochemistry and function in the myosin superfamily. *Curr Opin Cell Biol* 16, 61–67.
- De La Cruz EM, Sweeney HL, Ostap EM (2000). ADP inhibition of myosin V ATPase activity. *Biophys J* 79, 1524–1529.

- Dosé AC, Ananthanarayanan S, Moore JE, Burnside B, Yengo CM (2007). Kinetic mechanism of human myosin IIIA. *J Biol Chem* 282, 216–231.
- Dosé AC, Ananthanarayanan S, Moore JE, Corsa AC, Burnside B, Yengo CM (2008). The kinase domain alters the kinetic properties of the myosin IIIA motor. *Biochemistry* 47, 2485–2496.
- Dosé AC, Burnside B (2000). Cloning and chromosomal localization of a human class III myosin. *Genomics* 67, 333–342.
- Dosé AC, Burnside B (2002). A class III myosin expressed in the retina is a potential candidate for Bardet-Biedl syndrome. *Genomics* 79, 621–624.
- Dosé AC, Hillman DW, Wong C, Sohlberg L, Lin-Jones J, Burnside B (2003). Myo3A, one of two class III myosin genes expressed in vertebrate retina, is localized to the calycul processes of rod and cone photoreceptors and is expressed in the sacculus. *Mol Biol Cell* 14, 1058–1073.
- Drummond MC, Barzik M, Bird JE, Zhang DS, Lechene CP, Corey DP, Cunningham LL, Friedman TB (2015). Live-cell imaging of actin dynamics reveals mechanisms of stereocilia length regulation in the inner ear. *Nat Commun* 6, 6873.
- Ebrahim S, Avenarius MR, Grati M, Krey JF, Windsor AM, Sousa AD, Ballesteros A, Cui R, Millis BA, Salles FT, et al. (2016). Stereocilia-staircase spacing is influenced by myosin III motors and their cargos espin-1 and espin-like. *Nat Commun* 7, 10833.
- Forgacs E, Sakamoto T, Cartwright S, Belknap B, Kovács M, Tóth J, Webb MR, Sellers JR, White HD (2009). Switch 1 mutation S217A converts myosin V into a low duty ratio motor. *J Biol Chem* 284, 2138–2149.
- Galdeen SA, Stephens S, Thomas DD, Titus MA (2007). Talin influences the dynamics of the myosin VII-membrane interaction. *Mol Biol Cell* 18, 4074–4084.
- Geeves MA (2016). Review: The ATPase mechanism of myosin and actomyosin. *Biopolymers* 105, 483–491.
- Geeves MA, Perreault-Micale C, Coluccio LM (2000). Kinetic analyses of a truncated mammalian myosin I suggest a novel isomerization event preceding nucleotide binding. *J Biol Chem* 275, 21624–21630.
- Grati M, Yan D, Raval MH, Walsh T, Ma Q, Chakchouk I, Kannan-Sundhari A, Mittal R, Masmoudi S, Blanton SH, et al. (2016). MYO3A Causes Human Dominant Deafness and Interacts with Protocadherin 15-CD2 Isoform. *Hum Mutat* 37, 481–487.
- Greenberg MJ, Lin T, Shuman H, Ostap EM (2015). Mechanochemical tuning of myosin-I by the N-terminal region. *Proc Natl Acad Sci USA* 112, E3337–E3344.
- Heissler SM, Sellers JR (2016a). Kinetic adaptations of myosins for their diverse cellular functions. *Traffic* 17, 839–859.
- Heissler SM, Sellers JR (2016b). Various Themes of Myosin Regulation. *J Mol Biol* 428, 1927–1946.
- Holt JR, Pan B, Koussa MA, Asai Y (2014). TMC function in hair cell transduction. *Hear Res* 311, 17–24.
- Krey JF, Chatterjee P, Dumont RA, O’Sullivan M, Choi D, Bird JE, Barr-Gillespie PG (2020). Mechanotransduction-dependent control of stereocilia dimensions and row identity in inner ear hair cells. *Curr Biol* 30, 442–454.
- Kerber ML, Cheney RE (2011). Myosin-X: a MyTH-FERM myosin at the tips of filopodia. *J Cell Sci* 124, 3733–3741.
- Lanzetta PA, Alvarez LJ, Reinach PS, Candia OA (1979). An improved assay for nanomole amounts of inorganic phosphate. *Anal Biochem* 100, 95–97.
- Lelli A, Michel V, Boutet de Monvel J, Cortese M, Bosch-Grau M, Aghaie A, Perfettini I, Dont T, Avan P, El-Amraoui A, Petit C (2016). Class III myosins shape the auditory hair bundles by limiting microvilli and stereocilia growth. *J Cell Biol* 212, 231–244.
- Les Erickson F, Corsa AC, Dose AC, Burnside B (2003). Localization of a class III myosin to filopodia tips in transfected HeLa cells requires an actin-binding site in its tail domain. *Mol Biol Cell* 14, 4173–4180.
- Li J, He Y, Weck ML, Lu Q, Tyska MJ, Zhang M (2017). Structure of Myo7b/USH1C complex suggests a general PDZ domain binding mode by MyTH4-FERM myosins. *Proc Natl Acad Sci USA* 114, E3776–E3785.
- Li J, Liu H, Raval MH, Wan J, Yengo CM, Liu W, Zhang M (2019). Structure of the MORN4/Myo3a tail complex reveals MORN repeats as protein binding modules. *Structure* 27, 1366–1374 e3.
- Lin HW, Schneider ME, Kachar B (2005). When size matters: the dynamic regulation of stereocilia lengths. *Curr Opin Cell Biol* 17, 55–61.
- Manor U, Disanza A, Grati M, Andrade L, Lin H, Di Fiore PP, Scita G, Kachar B (2011). Regulation of stereocilia length by myosin XVa and whirlin depends on the actin-regulatory protein Eps8. *Curr Biol* 21, 167–172.
- Manor U, Grati M, Yengo CM, Kachar B, Gov NS (2012). Competition and compensation: dissecting the biophysical and functional differences between the class 3 myosin paralogs, myosins 3a and 3b. *Bioarchitecture* 2, 171–174.
- Manor U, Kachar B (2008). Dynamic length regulation of sensory stereocilia. *Semin Cell Dev Biol* 19, 502–510.
- Mazerik JN, Kraft LJ, Kenworthy AK, Tyska MJ (2014). Motor and tail homology 1 (Th1) domains antagonistically control myosin-1 dynamics. *Biophys J* 106, 649–658.
- Mazerik JN, Tyska MJ (2012). Myosin-1A targets to microvilli using multiple membrane binding motifs in the tail homology 1 (TH1) domain. *J Biol Chem* 287, 13104–13115.
- McGrath J, Roy P, Perrin BJ (2017). Stereocilia morphogenesis and maintenance through regulation of actin stability. *Semin Cell Dev Biol* 65, 88–95.
- Mecklenburg KL, Freed SA, Raval M, Quintero OA, O’Tousa JE (2015). Invertebrate and vertebrate class III myosins interact with MORN repeat-containing adaptor proteins. *PLoS One* 10, e0122502.
- Merritt RC, Manor U, Salles FT, Grati M, Dose AC, Unrath WC, Quintero OA, Yengo CM, Kachar B (2012). Myosin IIIB uses an actin-binding motif in its espin-1 cargo to reach the tips of actin protrusions. *Curr Biol* 22, 320–325.
- Moer RJ, Johnsrud DO, Thomas DD, Titus MA (2011). Characterization of a myosin VII MyTH/FERM domain. *J Mol Biol* 413, 17–23.
- Mooseker MS, Cheney RE (1995). Unconventional myosins. *Annu Rev Cell Dev Biol* 11, 633–675.
- Moreland ZaneG, Jiang Fangfang, Aguilar Carlos, Barzik Melanie, Gong Rui, Shams Arik, Faaborg-Andersen Christian, Werth JesseC, Harley Randall, Sutton DanielC, et al. (2021). Myosin-driven nucleation of actin filaments drives stereocilia development critical for hearing. *bioRxiv* 2021.07.09.451618.
- Nambiar R, McConnell RE, Tyska MJ (2009). Control of cell membrane tension by myosin-I. *Proc Natl Acad Sci USA* 106, 11972–11977.
- Nambiar R, McConnell RE, Tyska MJ (2010). Myosin motor function: the ins and outs of actin-based membrane protrusions. *Cell Mol Life Sci* 67, 1239–1254.
- Naoy M, Manor U, Sakaguchi H, Kachar B, Gov NS (2008). Protein localization by actin treadmill and molecular motors regulates stereocilia shape and treadmill rate. *Biophys J* 95, 5706–5718.
- Narayanan P, Chatterton P, Ikeda A, Ikeda S, Corey DP, Ervasti JM, Perrin BJ (2015). Length regulation of mechanosensitive stereocilia depends on very slow actin dynamics and filament-severing proteins. *Nat Commun* 6, 6855.
- Pardee JD, Spudich JA (1982). Purification of muscle actin. *Methods Enzymol* 85(Pt B), 164–181.
- Quintero OA, Moore JE, Unrath WC, Manor U, Salles FT, Grati M, Kachar B, Yengo CM (2010). Intermolecular autophosphorylation regulates myosin IIIa activity and localization in parallel actin bundles. *J Biol Chem* 285, 35770–35782.
- Quintero OA, Unrath WC, Stevens SM Jr, Manor U, Kachar B, Yengo CM (2013). Myosin 3A kinase activity is regulated by phosphorylation of the kinase domain activation loop. *J Biol Chem* 288, 37126–37137.
- Rehman AU, Bird JE, Faridi R, Shahzad M, Shah S, Lee K, Khan SN, Imtiaz A, Ahmed ZM, Riazuddin S, et al. (2016). Mutational spectrum of MYO15A and the molecular mechanisms of DFNB3 human deafness. *Hum Mutat* 37, 991–1003.
- Raval MH, Quintero OA, Weck ML, Unrath WC, Gallagher JW, Cui R, Kachar B, Tyska MJ, Yengo CM (2016). Impact of the Motor and Tail Domains of Class III Myosins on Regulating the Formation and Elongation of Actin Protrusions. *J Biol Chem* 291, 22781–22792.
- Rzadzinska AK, Nevalainen EM, Prosser HM, Lappalainen P, Steel KP (2009). Myosin VIIa interacts with Twinfilin-2 at the tips of mechanosensory stereocilia in the inner ear. *PLoS One* 4, e7097.
- Rzadzinska A, Schneider M, Noben-Trauth K, Bartles JR, Kachar B (2005). Balanced levels of Espin are critical for stereociliary growth and length maintenance. *Cell Motil Cytoskeleton* 62, 157–165.
- Salles FT, Merritt RC Jr, Manor U, Dougherty GW, Sousa AD, Moore JE, Yengo CM, Dosé AC, Kachar B (2009). Myosin IIIa boosts elongation of stereocilia by transporting espin 1 to the plus ends of actin filaments. *Nat Cell Biol* 11, 443–450.
- Schneider ME, Dosé AC, Salles FT, Chang W, Erickson FL, Burnside B, Kachar B (2006). A new compartment at stereocilia tips defined by spatial and temporal patterns of myosin IIIa expression. *J Neurosci* 26, 10243–10252.
- Siemankowski RF, Wiseman MO, White HD (1985). ADP dissociation from actomyosin subfragment 1 is sufficiently slow to limit the unloaded shortening velocity in vertebrate muscle. *Proc Natl Acad Sci USA* 82, 658–662.
- Tyska MJ, Mooseker MS (2002). MYO1A (brush border myosin II) dynamics in the brush border of LLC-PK1-CL4 cells. *Biophys J* 82, 1869–1883.

- Walsh T, Walsh V, Vreugde S, Hertzano R, Shahin H, Haika S, Lee MK, Kanaan M, King MC, Avraham KB (2002). From flies' eyes to our ears: mutations in a human class III myosin cause progressive nonsyndromic hearing loss DFNB30. *Proc Natl Acad Sci USA* 99, 7518–7523.
- Walsh VL, Raviv D, Dror AA, Shahin H, Walsh T, Kanaan MN, Avraham KB, King MC (2011). A mouse model for human hearing loss DFNB30 due to loss of function of myosin IIIA. *Mamm Genome* 22, 170–177.
- Weck ML, Grega-Larson NE, Tyska MJ (2017). MyTH4-FERM myosins in the assembly and maintenance of actin-based protrusions. *Curr Opin Cell Biol* 44, 68–78.
- Yang Y, Baboolal TG, Siththanandan V, Chen M, Walker ML, Knight PJ, Peckham M, Sellers JR (2009). A FERM domain autoregulates *Drosophila* myosin 7a activity. *Proc Natl Acad Sci USA* 106, 4189–4194.